Optical fiber in-line Mach–Zehnder interferometer based on dual internal mirrors formed by a hollow sphere pair

T. Y. Hu and D. N. Wang*

Department of Electrical Engineering, The Hong Kong Polytechnic University, Hung Hom, Kowloon, Hong Kong, China
**Corresponding author: eednwang@polyu.edu.hk*

Received May 2, 2013; revised July 15, 2013; accepted July 17, 2013;
posted July 18, 2013 (Doc. ID 189899); published August 7, 2013

We demonstrate a fiber in-line Mach–Zehnder interferometer based on dual internal mirrors formed by a hollow sphere pair and fabricated by femtosecond laser micromachining together with the fusion splicing technique. The hollow sphere surface adjacent to the fiber core can reflect part of the incident light beam to the air–cladding interface, where the light beam is reflected again before returning to the fiber core by another hollow sphere surface and recombining with the light beam remaining in the fiber core. Such an interferometer is miniature and robust, and is sensitive to environmental variations and allows simultaneous surrounding refractive index, temperature, and curvature measurement.

OCIS codes: (230.4040) Mirrors; (220.4000) Microstructure fabrication; (120.3180) Interferometry.
http://dx.doi.org/10.1364/OL.38.003036

The optical fiber in-line interferometer is an attractive photonic device because of its in-line nature, which enables convenient operation. Various types of fiber in-line interferometers have been demonstrated [1–11]; among them, the Mach–Zehnder interferometer (MZI) is featured with flexible structure and easy fabrication, while exhibiting high sensitivity when used for sensing. Currently, the fiber in-line MZI is mainly constructed by use of a long-period fiber grating (LPFG) pair [5,6], fiber tapers [7,8], mismatched fiber cores [9], and/or sandwiched structure consisting of single-mode fiber (SMF) and hollow-core fiber [10]. In such configurations, interference is produced by the fiber core mode and cladding mode, propagating along nearly the same path length. Owing to the small refractive index (RI) difference between the fiber core mode and the cladding mode, the size of the interferometer is usually large, especially when a small free spectral range (FSR) is required to improve the sensitivity. Although the MZI based on the open air cavity can effectively support a compact-sized device while maintaining high sensitivity, owing to the large RI difference between the fiber core and air, it inherently has poor robustness [12]. Recently, by use of the inner air cavity adjacent to the fiber core, a miniature and robust MZI has been demonstrated [13]. However, the isolated inner cavity structure limits its response to environmental variations such as the surrounding RI change.

Here we demonstrate a robust fiber in-line MZI based on dual internal mirrors that are formed by hollow sphere surfaces adjacent to the fiber core. One of its interesting features is that a compact device size corresponds to a large optical path difference (OPD) introduced by the interferometer and hence a small FSR. Moreover, as one of the interferometer arms reaches the air–cladding interface, sensitive response to the environmental variations can be achieved.

The operation principle of the MZI is illustrated in Fig. 1. Part of the input light beam in the fiber core follows path 1, is reflected by the first hollow sphere surface, and is incident on the interface between the fiber cladding and air, where it experiences another reflection before being reflected again at the second hollow sphere surface and returned to the fiber core to continue propagation. The rest of the input light beam in the fiber core propagates along path 2 and recombines with the light beam traveling in path 1 at the second hollow sphere surface, thus forming a fiber in-line MZI. In order to ensure a good interference fringe visibility and low insertion loss, total internal reflection needs to be achieved at every reflection surface described above.

The hollow sphere is fabricated by use of femtosecond (fs) laser micromachining, instead of chemical etching [14], together with the fusion splicing technique [13]. The fs laser pulses ($\lambda = 800$ nm) of 120 fs at a repetition rate of 1 kHz were focused onto the fiber by a 40× objective lens with an NA value of 0.66 and a working distance of 1.7 mm. A CCD camera was employed to monitor the fabrication process. A standard SMF-28 with effective RI of 1.4682 (at 1550 nm) was mounted on a computer-controlled three-dimensional translation stage with 40 nm resolution. A microsquare structure with a side length of ~22 μm and a largest depth of ~35 μm, centered at 20 μm away from the center of the cleaved fiber end facet, was inscribed by fs laser pulses with energy of ~3 μJ. The fiber tip with microstructure was then fusion spliced together with another cleaved SMF tip without microstructure to create a hollow sphere adjacent to the fiber core. The fusion splicer used was ERICSSO FSU975, and the fusing current and fusing duration employed were 16.2 mA and 2.0 s, respectively. With the help of a 20× microscope lens together with a CCD camera, the length of the fiber tip near the hollow sphere end could be controlled before being cleaved. The two fabricated fiber tips with a hollow sphere were fusion spliced together to form a fiber in-line MZI.

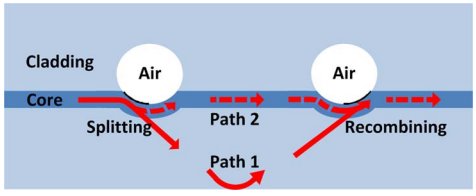

Fig. 1. Schematic diagram of the fiber in-line MZI.

The output intensity of the MZI is governed by

$$I = I_1 + I_2 + 2\sqrt{I_1 I_2}\cos\left(\frac{2\pi\Delta(nL)}{\lambda}\right), \quad (1)$$

where I_1 and I_2 represent the light intensity at the two interferometer arms, respectively, λ is the wavelength, and $\Delta(nL)$ is the OPD between the two interferometer arms. When the phase term satisfies the condition of $(2\pi\Delta(nL))/(\lambda) = (2m+1)\pi$, where m is an integer, the intensity dip appears at the wavelength

$$\lambda_{\text{dip}} = \frac{2\Delta(nL)}{2m+1}. \quad (2)$$

The FSR of the interference fringe dip of interest is determined by the OPD, $\Delta(nL)$, as

$$\text{FSR} = \frac{\lambda^2}{\Delta(nL)}. \quad (3)$$

The microscope images of the in-fiber hollow sphere pairs with different separations are demonstrated in Figs. 2(a)–2(e), together with their corresponding transmission spectra. It can be seen from this figure that the FSR of the device depends on the separation of the hollow sphere pair and an increased separation leads to an enlarged FSR. The main factors to determine the beam ratio split by the internal mirror and hence the output fringe visibility include the size and depth of the inscribed microstructure and the fusion time and current. It is found that when the hollow sphere diameter is between 55 and 58 μm, the largest possible fringe visibility can be obtained and the polarization effect on the visibility is not significant.

As illustrated in the inset of Fig. 2(f), assuming that the separation of the hollow sphere pair is $2x$, the distance between the fiber central axis and the air–cladding interface is y, and then the OPD between the two arms of the interferometer is $\Delta(nL) = 2(n_{\text{cl}}z - n_{\text{co}}x)$, where n_{cl} and n_{co} are the RI of fiber cladding and core, respectively, and $z = \sqrt{x^2 + y^2}$. When the separation is increased by $2\Delta x$, the induced OPD change will be approximately $2(n_{\text{cl}}\Delta z - n_{\text{co}}\Delta x) = 2n_{\text{cl}}\Delta x(\Delta z/\Delta x) - (n_{\text{co}}/n_{\text{cl}})$. Since $(\Delta z/\Delta x) = (x/z) < 1$, and then $(\Delta z/\Delta x) - (n_{\text{co}}/n_{\text{cl}}) < 0$, when the hollow sphere separation is increased, the OPD is decreased, resulting in an enlarged FSR.

The FSR values obtained in the experiments are displayed in Fig. 2(f). Compared with the theoretical curve shown in the same figure, good agreement is found, which verifies the operation of the MZI developed.

For the fiber in-line MZI reported so far, a relatively large cavity length is needed to produce a small FSR in order to improve the measurement accuracy and sensitivity, which results in a relatively large size of the device.

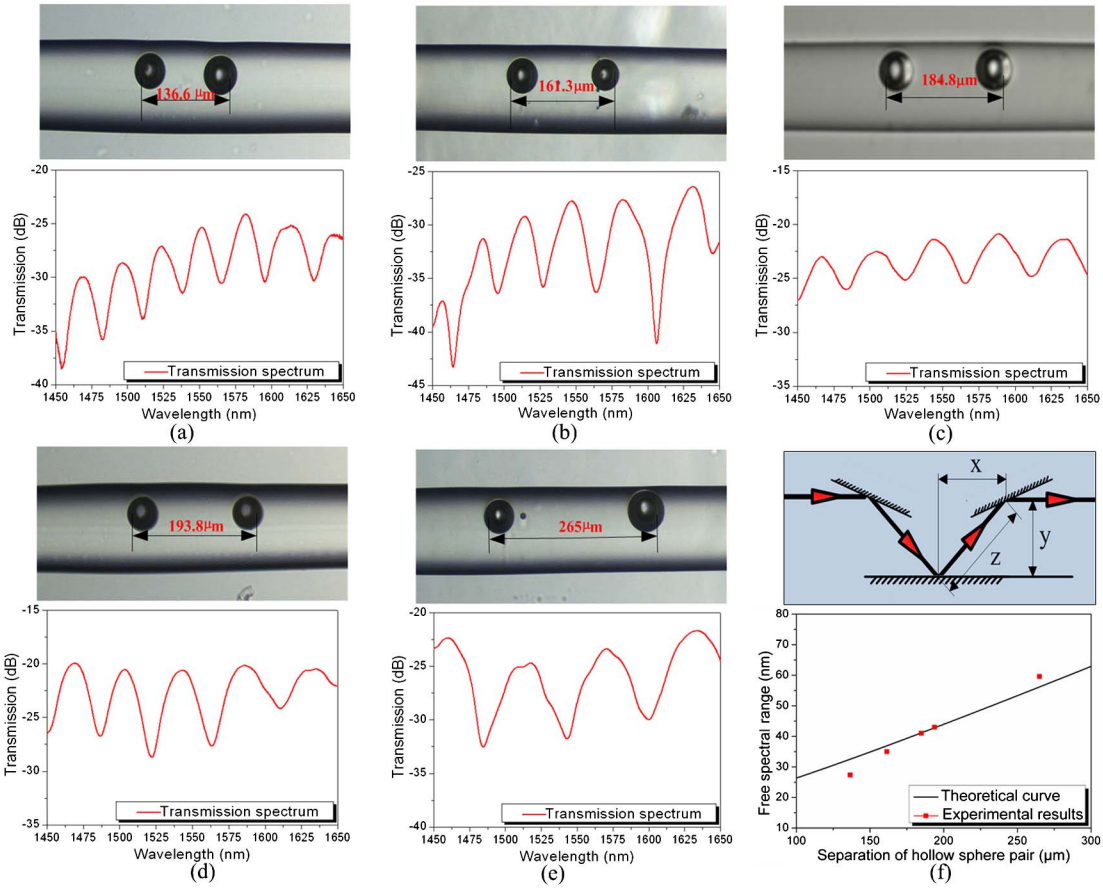

Fig. 2. Microscope image and corresponding spectrum for the hollow sphere pair with separation of (a) 136.6 μm, (b) 161.3 μm, (c) 184.8 μm, (d) 193.8 μm, and (e) 265 μm. (f) FSR versus the separation of the hollow sphere pair. Inset shows the path of the light reflected by the hollow sphere pair.

It is interesting to notice that to obtain a small FSR in our device, the separation of the hollow sphere pair should be reduced; i.e., a more compact device size can be realized, when compared with other fiber in-line MZIs.

In the axial strain measurement, the device sample with a hollow sphere separation of 193.8 μm was fixed on two translation stages. The dip wavelengths near 1523 nm in the transmission spectra corresponding to different axial strain values are displayed in the inset of Fig. 3, where a blue shift of fringe dip wavelength appears. Figure 3 shows the variation of dip wavelength with the axial strain in the range between 0 and 2700 με, where the sensitivity obtained is −1.44 pm/με, which is slightly higher than that of the fiber Bragg grating (FBG) [15,16]—however, with a largely reduced device size. The wide strain measurement range up to 2700 με also indicates the robustness of the device.

From Eq. (2), we have $\lambda_{\text{dip}} = (2\Delta(nL))/(2m+1) = (4/2m+1)(n_{\text{cl}}z - n_{\text{co}}x)$; the dip wavelength shift due to the change of axial strain can then be expressed as

$$\begin{aligned}\delta\lambda_{\text{dip}} &= \frac{4}{2m+1}[(n_{\text{cl}}+\delta n)(z+\Delta z) - (n_{\text{co}}+\delta n)(x+\Delta x)] \\ &\quad - \frac{4}{2m+1}(n_{\text{cl}}z - n_{\text{co}}x) \\ &\approx \frac{4}{2m+1}(n_{\text{cl}}\Delta z + z\delta n - n_{\text{co}}\Delta x - x\delta n) \\ &= \frac{4}{2m+1}\left[n_{\text{cl}}\Delta x\left(\frac{x}{z} - \frac{n_{co}}{n_{cl}}\right) + (z-x)\delta n\right], \end{aligned} \tag{4}$$

where δn is the RI change induced by the increased axial strain and has a negative value. Since $(x/z) - (n_{\text{co}}/n_{\text{cl}}) < 0$, an increase of axial strain would result in a blue shift of the dip wavelength.

The dip wavelength shift with the temperature variation is demonstrated in Fig. 4, where the inset shows the transmission spectra of the same device sample used in the axial strain test, at different temperatures. A fringe dip near ~1523 nm at room temperature was found to experience a red shift with the increase of temperature. The temperature sensitivity obtained is ~9.8 pm/°C, close to that of the FBG. Following the same analysis procedure used in deriving Eq. (4), the dip wavelength shift due to the temperature increase can be expressed as

$$\begin{aligned}\delta\lambda_{\text{dip}} &= \frac{4}{2m+1}\left[n_{\text{cl}}\Delta x\left(\frac{x}{z} - \frac{n_{\text{co}}}{n_{\text{cl}}}\right) + (z-x)\delta n_T\right] \\ &\approx \frac{4}{2m+1}(z-x)\delta n_T, \end{aligned} \tag{5}$$

where Δx is induced by material thermal expansion and δn_T denotes the change in the effective RI of silica, due to the thermal-optical effect. The thermal-optical effect plays the dominant role in determining the dip wavelength shift, as the thermo-optic coefficient (7.8×10^{-6}) is much larger than the thermal expansion coefficient (4.1×10^{-7}) in silica. Thus, when the temperature is increased, a red shift of dip wavelength appears, as indicated by Eq. (5).

The device sample with hollow sphere separation of 265 μm was tested for RI sensing to verify its response to external environment. The device was immersed in a series of RI liquids (from Cargille Laboratories) in the RI range of 1.30–1.44 (at 489.3 nm) with an interval of 0.02. Each time after the measurement, the fiber device

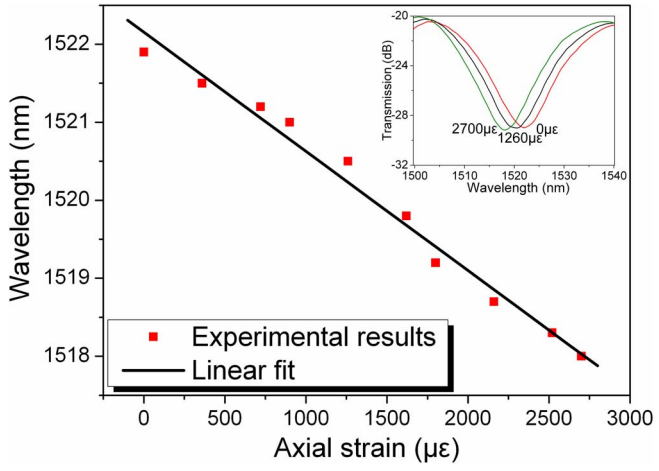

Fig. 3. Fringe dip wavelength shift with applied axial strain. Inset shows the transmission spectra of the device at different strains.

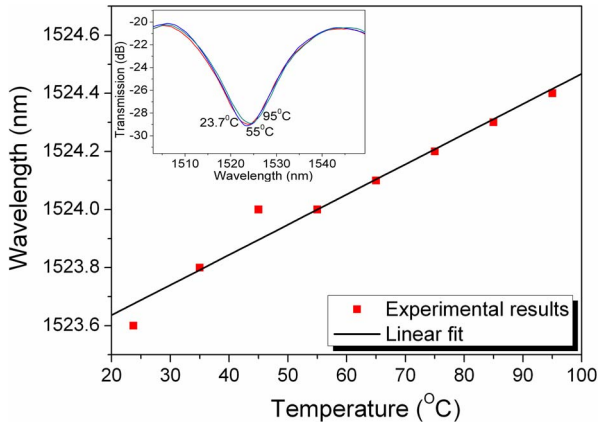

Fig. 4. Fringe dip wavelength shift with temperature variation. Inset shows the transmission spectra of the device at different temperatures.

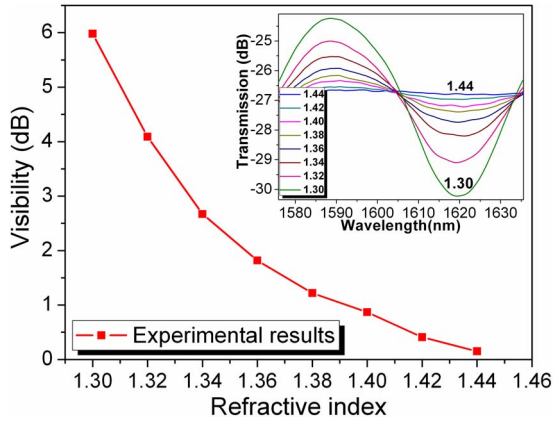

Fig. 5. Variation of the output fringe visibility with external RI. Inset shows the transmission spectra of the device at different external RI values.

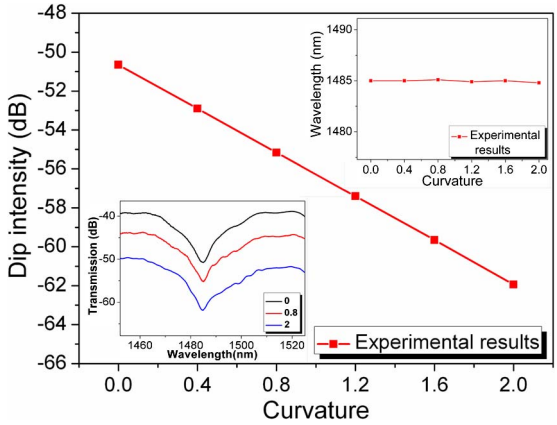

Fig. 6. Dip wavelength intensity versus curvature. The upper inset shows the fringe dip wavelength versus curvature, and the lower shows the transmission spectra of the device at curvature ratios of 0, 0.8, and 2 m^{-1}, respectively.

was rinsed with methanol carefully until the original spectrum (i.e., the reference spectrum) could be restored and no residue liquid was left on the fiber surface. The variation of the fringe visibility with the RI change is shown in Fig. 5, where the inset reveals the transmission spectra within the wavelengths range between 1575 and 1635 nm. It can be found from the figure that the visibility of the output fringe pattern critically depends on the RI and is gradually decreased when the RI value is increased from 1.33 and approaches to zero when the RI value reaches 1.44. This is due to the fact that when the RI value of the surrounding environment becomes nearly the same as that of the fiber cladding, the light beam would directly come out from the optical fiber and enter into the surrounding medium without reflection. The highest sensitivity obtained is ~ – 75.6 dB/RIU (RI unit) at the RI value of 1.30.

The device sample with hollow sphere separation of 265 μm was also tested in the bending measurement. The sample was closely attached on the central part of a flexible steel ruler fixed between two translation stages, which was moved inward to induce a bend in the ruler and, hence, in the fiber device. The sensor curvature is given by $C = 12d/l^2$ [17], where l is the distance between the edges of the two stages, and d is the bending displacement at the center of the fiber in-line MZI. As shown in Fig. 6, the fringe dip wavelength close to 1485 nm does not shift with curvature. This can be explained by the fact that there is essentially no change in the optical path lengths of the two interferometer arms when the curvature is varied, and hence no OPD change is generated for such a small device length. However, the dip intensity is decreased with the increase of curvature.

It is interesting to notice that in our device, the change in surrounding RI leads to a change in output fringe visibility, the variation in temperature only shifts the fringe dip wavelength, and the change in curvature merely causes a change in fringe dip intensity; i.e., three-parameter sensing can be simultaneously achieved, and thus the temperature cross sensitivity can be eliminated.

In conclusion, the surfaces of the hollow sphere pair positioned adjacent to the fiber core play the role of fiber internal mirrors, which effectively reflect part of the incident light beam in the fiber core to the air–cladding interface, where, after experiencing another reflection, the light beam returns to the fiber core, and recombines with the light beam remaining in the fiber core to form a fiber in-line MZI. Such an inner structure-based fiber device is miniature, robust, suitable for high-accuracy measurement, sensitive to the surrounding environment, and free of temperature cross sensitivity, thus exhibiting high potential in versatile photonic applications.

This work was supported by Hong Kong Polytechnic University Research grants 4-ZZE3 and 4-ZZE6.

References

1. Y. J. Yao, M. Deng, D. W. Duan, X. C. Yang, T. Zhu, and G. H. Cheng, Opt. Express **15**, 14123 (2007).
2. J. Villatoro, V. Finazzi, G. Coviello, and V. Pruneri, Opt. Lett. **34**, 2441 (2009).
3. L. B. Yuan, J. Yang, Z. Liu, and J. Sun, Opt. Lett. **31**, 2692 (2006).
4. C. R. Liao, D. N. Wang, M. Wang, and M. Yang, IEEE Photon. Technol. Lett. **24**, 2060 (2012).
5. J. H. Lim, H. S. Jang, K. S. Lee, J. C. Kim, and B. H. Lee, Opt. Lett. **29**, 346 (2004).
6. J. F. Ding, A. P. Zhang, L. Y. Shao, J. H. Yan, and S. L. He, IEEE Photon. Technol. Lett. **17**, 1247 (2005).
7. J. Villatoro, V. P. Minkovich, and D. Monzón-Hernández, IEEE Photon. Technol. Lett. **18**, 1258 (2006).
8. P. Lu, L. Men, K. Sooley, and Q. Chen, Appl. Phys. Lett. **94**, 131110 (2009).
9. Z. Tian, S. S.-H. Yam, and H. Loock, IEEE Photon. Technol. Lett. **20**, 1387 (2008).
10. Y. Jung, S. Lee, B. H. Lee, and K. Oh, Opt. Lett. **33**, 2934 (2008).
11. P. L. Swart, Meas. Sci. Technol. **15**, 1576 (2004).
12. Y. Wang, M. Yang, D. N. Wang, S. Liu, and P. Lu, J. Opt. Soc. Am. B **27**, 370 (2010).
13. T. Y. Hu, Y. Wang, C. R. Liao, and D. N. Wang, Opt. Lett. **37**, 5082 (2012).
14. E. Cibula and D. Donlagic, Opt. Express **18**, 12017 (2010).
15. C. Chen, A. Laronche, G. Bouwmans, L. Bigot, Y. Quiquempois, and J. Albert, Opt. Express **16**, 9645 (2008).
16. N. Liu, Y. Li, Y. Wang, H. Wang, W. Liang, and P. Lu, Opt. Express **19**, 13880 (2011).
17. Y. P. Wang, Y. J. Rao, Z. L. Ran, T. Zhu, and X. K. Zeng, Opt. Lasers Eng. **41**, 233 (2004).